Original article

Supramolecular prodrug inspiried by the *Rhizoma Coptidis-Fructus Mume* herbal pair alleviated inflammatory diseases by inhibiting pyroptosis

Wenhui Qian [a,1], Bei Zhang [a,1], Ming Gao [b], Yuting Wang [a], Jiachen Shen [a], Dongbing Liang [a], Chao Wang [a], Wei Wei [a], Xing Pan [a], Qiuying Yan [c], Dongdong Sun [c,***], Dong Zhu [a,**], Haibo Cheng [c,*]

[a] *School of Pharmacy, Nanjing University of Chinese Medicine, Nanjing, 210023, China*
[b] *Department of Pharmacy, Jinling Hospital, Nanjing University School of Medicine, Nanjing, 210002, China*
[c] *Jiangsu Collaborative Innovation Center of Traditional Chinese Medicine Prevention and Treatment of Tumor, Nanjing, 210023, China*

ARTICLE INFO

ABSTRACT

Sustained inflammatory responses are closely related to various severe diseases, and inhibiting the excessive activation of inflammasomes and pyroptosis has significant implications for clinical treatment. Natural products have garnered considerable concern for the treatment of inflammation. Huanglian-Wumei decoction (HLWMD) is a classic prescription used for treating inflammatory diseases, but the necessity of their combination and the exact underlying anti-inflammatory mechanism have not yet been elucidated. Inspired by the supramolecular self-assembly strategy and natural drug compatibility theory, we successfully obtained berberine (BBR)-chlorogenic acid (CGA) supramolecular (BCS), which is an herbal pair from HLWMD. Using a series of characterization methods, we confirmed the self-assembly mechanism of BCS. BBR and CGA were self-assembled and stacked into amphiphilic spherical supramolecules in a 2:1 molar ratio, driven by electrostatic interactions, hydrophobic interactions, and $\pi-\pi$ stacking; the hydrophilic fragments of CGA were outside, and the hydrophobic fragments of BBR were inside. This stacking pattern significantly improved the anti-inflammatory performance of BCS compared with that of single free molecules. Compared with free molecules, BCS significantly attenuated the release of multiple inflammatory mediators and lipopolysaccharide (LPS)-induced pyroptosis. Its anti-inflammatory mechanism is closely related to the inhibition of intracellular nuclear factor-kappaB (NF-κB) p65 phosphorylation and the noncanonical pyroptosis signalling pathway mediated by caspase-11.

1. Introduction

A sustained inflammatory response contributes to the development and progression of serious diseases, including tumours, cardiovascular diseases, neurodegenerative diseases, obesity, and diabetes [1,2]. Macrophage activation plays a pivotal role in the tissue inflammatory response, and these innate immune cells eliminate invading pathogens through various mechanisms, including phagocytosis and direct killing [3,4]. Inflammasomes, large intracellular multiprotein complexes in macrophages, are crucial to innate immunity. Inflammasomes are in response to pathogen-associated molecular patterns (PAMPs) and damage-associated molecular patterns (DAMPs) [5,6]. A variety of inflammasomes have been identified, with nucleotide-binding oligomerization domain (NOD)-like receptor family pyrin domain-containing 3 (NLRP3) being the most characterized [7–9]. Upon recognition of PAMPs or DAMPs, the nuclear factor-kappaB (NF-κB) signalling pathway is activated, contributing to the transcriptional upregulation of inflammasome-related components, including caspase-4/5/11 (a cysteine-dependent aspartate-directed protease), caspase-1, and NLRP3 [8,10,11]. This activation culminates in the release of inflammatory factors, including interleukin-1β (IL-1β)

and IL-18, contributing to pyroptosis. Pyroptosis is an intense inflammatory response often characterized by cellular swelling, rupture, and excessive release of lactate dehydrogenase and proinflammatory cytokines. Consequently, the excessive activation of inflammasomes and pyroptosis is believed to play a significant role in the pathogenesis of various inflammatory diseases, making the inhibition of pyroptosis crucial in treating these conditions [12].

Currently, only a limited number of drugs can inhibit caspase-4/5/11-mediated pyroptosis via the noncanonical pathway [13]. Recently, there has been increased interest in plant-derived natural products for treating inflammatory diseases [14,15] because of their overuse and resistance to broad-spectrum antibiotics. Consequently, natural medicinal plants offer substantial research potential, particularly given the growing recognition of the synergistic applications of traditional Chinese medicine (TCM) in clinical practice [16]. The compatibility of natural compounds represents a distinctive treatment model in TCM, with thousands of years of practice in China yielding numerous inspiring clinical experiences [17,18]. Among the array of compatible natural products, a particular class of drug combination has garnered significant attention. This combination involves two specific natural drugs, commonly referred to as an "herbal pair" in TCM. A "herbal pair" constitutes the most fundamental and straightforward form of compatibility in TCM therapy [19]. In an "herbal pair", two herbs possess similar therapeutic components that, when combined, produce synergistic effects. Individually, a single component may be ineffective, yet it can become effective within the herbal pair [20].

The Huanglian Wumei decoction (HLWMD), documented in the ancient Chinese herbal medicine book "Shanghanlun" (Treatise on Febrile Diseases), is extensively used to treat various inflammatory diseases, including ulcerative colitis, diabetes, and irritable bowel syndrome, with notable therapeutic success [21–23]. *Rhizoma Coptidis* and *Fructus Mume* constitute the classical herbal pair used for this purpose. Together, these two herbs significantly enhance the efficacy of the formula in clearing heat, inhibiting bacterial growth, and reducing inflammation. *Rhizoma Coptidis*, a TCM, exhibits a range of pharmacological activities, including antibacterial, anti-inflammatory, hypoglycaemic, and anticancer activities [24,25]. Its primary active component is berberine (BBR). *Fructus Mume* is the dried, near-ripe fruit of *Prunus mume* (Sib.) Sib. et Zucc of the Rosaceae family. Contemporary pharmacological research indicates that *Prunus mume* possesses many therapeutic treatments, such as antibacterial and anti-inflammatory agents, as well as intestinal flora modulation, antioxidant activity, and antitumour properties [26]. Chlorogenic acid (CGA) is an important natural organic acid with pharmacological activity in the plums and kernels of fruits. *Rhizoma Coptidis-Fructus Mume* (RC-FM) pairing is a hallmark of the HLWMD [27]. Although such synergistic effects are common in clinical practice, the underlying essential molecular mechanisms of this combination remain to be elucidated. Meanwhile, the exploration and development of supramolecules with self-assembling capabilities have surged in recent years [28,29]. One novel approach is the binary self-assembly system of supramolecules, which entails the carrier-free self-assembly of two or more small chemicals via various noncovalent interactions, including hydrogen bonding, electrostatic interactions, charge transfer, dispersion, hydrophobic interactions, and stacking, resulting in complex and organized molecules with targeted functions [30,31]. Supramolecular phenomena frequently occur in natural herbs due to the multitude of components involved in the decoction process [32,33].

Here, inspired by supramolecular self-assembly strategies and the theory of natural drug compatibility, we developed a new approach to elucidate the synergistic anti-inflammatory effects of the classical RC-FM pair (Scheme 1). First, we successfully obtained self-assembling natural phytochemicals from a decoction of the classic HLWMD. Preliminary infrared (IR) and ultraviolet-visible (UV-vis) spectroscopy revealed that the compound primarily consists of BBR and CGA, the two active constituents of the classical RC-FM pair. To further investigate the self-assembly mechanism of the obtained molecule, BBR and CGA were combined to form structural units termed BBR-CGA supramolecular (BCS). Through a series of characterization methods, such as IR spectroscopy and nuclear magnetic resonance (NMR) hydrogen spectroscopy, we discovered that BBR and CGA initially interact via electrostatic interactions at a 2:1 molar ratio to form a U-shaped planar structural unit. Then, driven by $\pi-\pi$ stacking and hydrophobic interactions, the U structural units further self-assemble and stack to form amphiphilic spherical supramolecules with hydrophilic exteriors and hydrophobic interiors. Concurrently, the formation of amphiphilic BCS significantly augmented the anti-inflammatory effects of BBR and CGA alone, markedly inhibiting the release of lipopolysaccharide (LPS)-induced intracellular reactive oxygen species (ROS) and the inflammatory cytokines IL-1β and IL-18. Moreover, our research work demonstrated that BCS can mitigate macrophage pyroptosis under inflammatory conditions. To further investigate the molecular mechanism by which BCS inhibits pyroptosis and ameliorates inflammatory diseases, we employed RNA sequencing (RNA-seq) and Western blotting to analyse the molecular effects of BCS. RNA-seq analysis revealed that genes differentially expressed following BCS treatment were predominantly enriched in the NOD-like receptor signalling pathway. Furthermore, we discovered that BCS can decelerate the release of salient inflammatory regulators by impeding the phosphorylation of NF-κB p65 in macrophages. BCS may also exert its anti-inflammatory effect by obstructing the activation of the caspase-4/5/11-mediated noncanonical pathway. BCS may also attenuate pyroptosis by blocking caspase-4/5/11-mediated activation of noncanonical pathways, thereby alleviating the development of inflammatory-type diseases. Our findings, for the first time, explain and clarify the scientific connotations of TCM compatibility from the perspective of self-assembly and synergistic effects and provide a new idea and strategy for elucidating the mechanism of multiherbal combinations of TCM.

2. Materials and methods

2.1. Materials

BBR and CGA were obtained from Shanghai Macklin Biochemical Co., Ltd. NaHCO$_3$ was supplied by Sinopharm Chemical Reagent Co., Ltd. (Beijing, China). Dulbecco's modified eagle's medium (DMEM), phosphate-buffered saline (PBS) containing 0.9% NaCl, and the penicillin-streptomycin solution were purchased from Thermo Fisher Scientific Inc. (Waltham, MA, USA). LPS was acquired from Solarbio Life Science Co., Ltd. (Beijing, China). Fetal bovine serum (FBS) and the primers for this study were purchased from Sangon Biotech (Shanghai, China) Co., Ltd.. The Cell Counting Kit-8 (CCK-8) was purchased from Nanjing Vazyme Biotech Co., Ltd. (Nanjing, China). Antibodies for P65 and beta-actin, along with horseradish peroxidase (HRP)-conjugated secondary antibodies, were sourced from Proteintech Group (Wuhan, China). Phospho-NF-κB p65 and glyceraldehyde-3-phosphate dehydrogenase (GAPDH) antibodies were purchased from Cell Signaling Technology (Beverly, MA, USA) and caspase-11 antibody was supplied by Abcam (Cambridge, UK). Ultrapure water was produced using a Milli-Q-RO4 water purification system (Millipore Simplicity; Millipore, Boston, MA, USA). All the reagents were utilized as provided without further purification for this study.
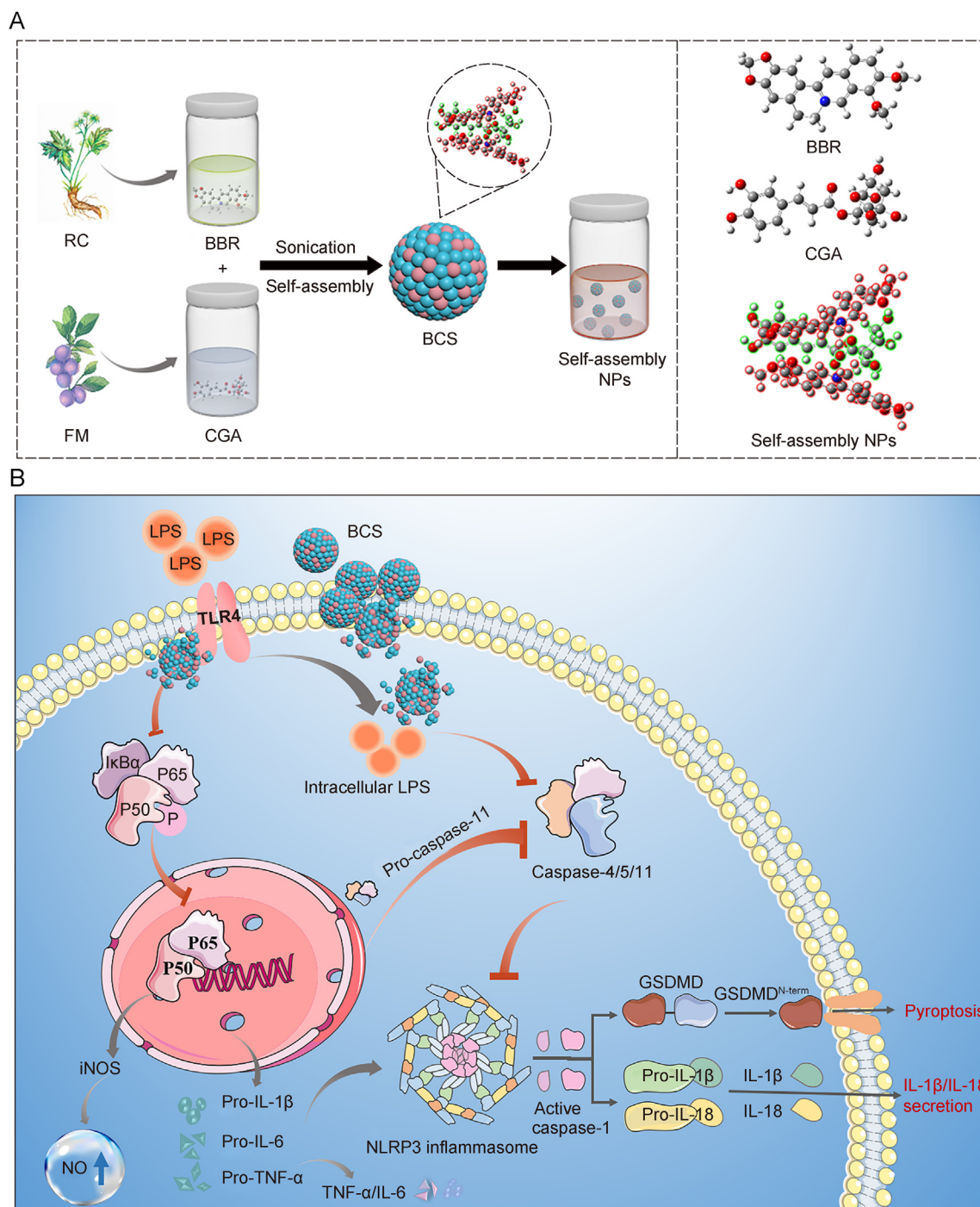
Scheme 1. Schematic representation of (A) the self-assembly and (B) the anti-inflammatory mechanisms of the berberine (BBR) and chlorogenic acid (CGA) supramolecular (BCS). NPs: nanoparticles; LPS: lipopolysaccharide; TLR4: Toll-like receptor 4; IκBα: nuclear factor of kappa light polypeptide gene enhancer in B-cells inhibitor alpha; iNOS: inducible nitric oxide (NO) synthase; IL: interleukin; TNF-α: tumor necrosis factor alpha; NLRP3: nucleotide-binding oligomerization domain (NOD)-like receptor family pyrin domain-containing 3; GSDMD: gasdermin D.

2.2. Preparation of BCS

BCS were prepared by a one-step self-assembly process. Briefly, 36 mg of CGA aqueous solutions were mixed with BBR solution at a 1:1 molar ratio at 60 °C while being vigorously stirred for 30 min. Then, aqueous solutions were adjusted with sodium bicarbonate (5 mg/mL) to pH 7.0−7.5. The solution was dialyzed against deionized water for 12 h after being sonicated for 1 h (molecular weight cutoff (MWCO) = 3.0 kDa). Finally, the solution was lyophilized to obtain BCS powder.

2.3. Characterization of self-assembly supramolecular

The micromorphology of BCS supramolecular was characterized by transmission electron microscopy (TEM), nanoparticle (NP) tracking analysis (NTA), and dynamic light scattering (DLS),

respectively. The UV-vis and fluorescence spectroscopy measurements were performed on a multi-function reader (Tecan Infinite M200-Pro; Tecan, Mannedorf, Switzerland). Fourier transform-IR (FT-IR) spectroscopy was obtained with the KBr method. ^{1}H NMR spectra were recorded on a 500 MHz spectrometer (Bruker, Billerica, MA, USA) to make sure the self-assembly units are forming.

2.4. Isothermal titration calorimetry (ITC) experiments

The GE MicroCal iTC200 (Malvern, Worcestershire, England) was used to perform the thermodynamic measurement. In the first titration, the sample cell was filled with deionized water, and the blank control group (I1) was titrated with CGA aqueous solution (2 mM). In the second titration, the sample cell was BBR aqueous solution (0.2 mM), and in the experimental group (I2), CGA (2 mM) was used to de-titrate BBR aqueous solution (0.2 mM). The final date was corrected by subtracting the data of the blank control group (I2-I1), and the Origin software in the instrument was used to fit the corrected data into the one-site binding model according to the thermodynamic equation. And the relevant thermodynamic parameters were finally calculated.

2.5. Hemolysis assay

Hemolysis analysis was carried out as described previously [32]. Briefly, fresh rat blood was collected into tubes and prepared into a 20% solution. Each sample was incubated with a 20% erythrocyte solution at 37 °C for 4 h, the red blood cell (RBC) suspension was detected at 540 nm by a microplate reader:

$$\text{Hemolysis rate (\%)} = (OD_{NPs} - OD_{blank})/(OD_{H2O} - OD_{blank}) \times 100$$

2.6. In vitro drug release and cellular uptake assay

Dialysis method was adopted to simulate the *in vitro* drug release of BCS and BBR. The sealed dialysis membrane (MWCO = 2.0 kDa) was placed in the medium containing phosphate buffer solution, and 1 mL was taken from the released external solution at 1, 2, 4, 6, 8, 10, 12, 16, and 24 h, respectively, for UV absorbance determination at 345 nm:

$$\text{Drug release (\%)} = (OD_{BCS} - OD_{blank})/(OD_{BBR} - OD_{blank}) \times 100$$

Fluorescein isothiocyanate (FITC) labeling was performed according to the methods in the literature. In brief, BCS (20 μM, 1 mL) was incubated with FITC (20 μg/mL, 0.2 mL) at 4 °C overnight. The free FITC was removed by ultrafiltration to obtain FITC@BCS. Drug-containing medium was added to RAW264.7 cells at different time points and incubated in the cell incubator for 3, 6, 9, and 12 h, respectively. The drug containing medium was removed by suction, washed three times with PBS, and then 1 mL of paraformaldehyde solution was added to it, and fixed at 37 °C for 20 min. After washing three times with PBS, 500 μL of 4′,6-diamidino-2-phenylindole (DAPI) solution (Ex = 340 nm and Em = 488 nm) was added to cover the cell surface, fixed at 37 °C in the dark for 5 min, washed three times with PBS, added 300 μL of anti-fluorescence quench agent, and detected by fluorescence microscopy (Ex = 470 nm and Em = 525 nm) at 4 °C in the dark.

2.7. Cell culture and cytotoxic effect

RAW264.7 cells (10^4 cells per well) were inoculated in 96 wells with varied concentrations of BBR, CGA, and BCS, and the incubation period was 24 or 48 h. The supernatant was discarded, and 100 μL of DMEM containing 10% CCK-8 was substituted. After incubation for 1 h, a microplate reader was used to measure the optical absorbance at 450 nm: cell survival rate (%) = OD_{sample}/$OD_{blank} \times 100$.

2.8. ROS and nitric oxide (NO) assay

The 2′,7′-dichlorofluorescein diacetate (DCFH-DA) assay was adopted to determine the intracellular ROS generation, and NO levels were determined using Griess reagent (Beyotime Biotechnology, Shanghai, China). RAW264.7 cells were inoculated with or without drugs for 24 h, with or without LPS (1 μg/mL). Then, 50 μL of culture medium blended with 50 μL of Griess reagent and a microplate reader (Tecan Infinite M200-Pro; Tecan) were used to detect the NO levels at 5440 nm. After being washed three times, DCFH-DA was allowed to incubate with the cells for 30 min at 37 °C, washed for three times. Then, cells were examined by the laser scanning confocal microscopy and a microplate reader was simultaneously detected (Ex = 488 nm and Em = 525 nm).

2.9. Quantitative real time reverse transcription-polymerase chain reaction (qRT-PCR)

RAW264.7 cells were pretreated with drugs for 24 h induced with 1 μg/mL LPS or not. Total RNA was extracted from the cells and the reverse transcription reaction was formed according to the manufacturer's protocol. Details of the primer sequences are in Table S1. The amplification program for the qRT-PCR was done with the CFX Connect™ Real-Time PCR System (Bio-Rad Laboratories, Inc., Hercules, CA, USA).

2.10. Enzyme-linked immunosorbent assay (ELISA) assay of secreted IL-1β and IL-18

The levels of IL-1β and IL-18 secreted by RAW264.7 cells for 24 h induced with 1 μg/mL LPS or not were determined on culture supernatants using the mouse IL-1β and IL-18 kits, respectively, according to the manufacturer's instructions. Readings were performed using a microplate reader (Tecan Infinite M200-Pro; Tecan), and metabolite levels were quantified against the kit standard curves and expressed as pg/mL. Cells were counted through the trypan blue exclusion method using the TC20 Automated Cell Counter (Bio-Rad Laboratories, Inc.). All the experiments were performed in triplicate.

2.11. Cell death assay

Lytic cell death was determined by propidium iodide (PI) incorporation or lactic acid dehydrogenase (LDH) release. Briefly, cells were seeded in 96-well plates and stimulated with 1 μg/mL LPS or not. Subsequently, the cells were treated with for 24 h. PI (2 mg/mL) solution together with Hoechst 33342 (5 mg/mL) was applied to measure the percentage of lytic cell death. Cells were observed immediately by live imaging with a fluorescence microscope (Leica, Wetzlar, Germany). Scutellarin's effects on intracellular LPS-induced lytic cell death were also measured by LDH release using lactate dehydrogenase cytotoxicity assay kit, according to instructions of the manufacturer (Beyotime Biotechnology).

2.12. High-throughput messenger RNA (mRNA)-sequence and data analysis

A stranded mRNA library was prepared for sequencing mRNA and generating stranded mRNA information. Three transcriptome

libraries (control, model, and BCS-treated groups) were constructed to perform RNA-seq, which was carried by Gene Denovo Biotech Co., Ltd. (Guangzhou, China). Thresholds of $P < 0.05$ and false discovery rate (FDR) $\leq$ 0.05 were used to select differentially expressed genes (DEGs). The significant genes were subjected to Kyoto Encyclopedia of Genes and Genomes (KEGG) pathway analysis.

2.13. Western blotting analysis

RAW264.7 cells were treated with drugs for 24 h induced with 1 μg/mL LPS or not. The cells were lysed and the protein concentration was determined by the bicinchoninic acid assay (BCA) assay kit (Beyotime Biotechnology). An equal amount of protein was subjected to electrophoresed on a 10% polyacrylamide gel and then transferred to the polyvinylidene fluoride (PVDF). After being blocked for 1 h with 5% skimmed milk, the PVDF incubated at 4 °C overnight with primary antibodies. Then the PVDF incubated for 2 h at room temperature with secondary antibodies conjugated with HRP. Protein bands were visualized by the BeyoECL Star (Yeasen Biotechnology, Shanghai, China).

2.14. Statistical treatment

Unless otherwise specified, all the samples were repeated three times and the error bars were calculated as the standard deviation (SD) of three independent experiments ($n = 3$). GraphPad Prism 7.0 was used to analyse the original data.

3. Results and discussion

3.1. Acquisition of self-assembling chemicals from HLWMD

Concentrated HLWMD was prepared using the traditional decoction method, and self-assembling phytochemicals were isolated via dialysis. Owing to the complex composition of HLWMD, the chemical particles in the decoction varied in size and potency. We utilized TEM to observe the micromorphology of the phytochemicals (Fig. S1A). The particle size distribution of the sample was 281.2 ± 18.9 nm (Fig. S1B). UV-vis absorption and FT-IR spectroscopy were conducted to analyse the phytochemical properties (Figs. S1C and D). The absorption spectrum in Fig. S1C revealed that the self-assembled NPs in the decoction exhibited absorption peaks corresponding to BBR at 228, 345, and 422 nm and a shoulder peak similar to that of CGA at 218 and 324 nm. IR spectroscopy indicated that the peak of the NPs was similar to that of CGA (1685.55 cm^{-1}) near 1701.20 cm^{-1} and that of BBR (1506.16 cm^{-1}) at 1506.20 cm^{-1}. These findings suggested that the phytochemicals in HLWMD may predominantly arise from the self-assembly of BBR and CGA.

3.2. Structural characteristics and self-assembly preparation of BCS

Inspired by the compatibility theory of natural compounds and to further investigate the self-assembling mechanism of natural chemicals in HLWMD and the specific mechanism of clinical anti-inflammatory treatment, we prepared BBR-CGA-active molecules by a one-step self-assembly process in accordance with the content ratio of BBR and CGA in the self-assembled natural chemicals isolated from HLWMD. Briefly, self-assembled BCS was prepared at 60 °C with a molar ratio of BBR to CGA (BBR:CGA = 1:1) in aqueous solution under vigorous stirring to obtain a homogeneous solution. The micromorphology of the BCS was characterized by TEM and NTA. TEM images (Figs. 1A and B) revealed that BBR and CGA self-assembled into a spheroid macromolecule with a size of 98.3 ± 15.5 nm, which was consistent with the results obtained for

NTA (with a particle size of 84 nm) (Fig. 1C). In addition, the zeta potential of the BCS was −16.3 mV, indicating the excellent stability of this supermolecule (Fig. S2).

UV-vis, FT-IR spectroscopy, and fluorescence assays were performed to demonstrate the properties of the self-assemblies. The UV-vis absorption spectra of BCS and the monomers were measured in the range of 200−500 nm (Fig. 1D). All the features of BBR (λ_{max} = 228, 264, and 345 nm) and CGA (λ_{max} = 218 and 324 nm) were included in the characteristic absorption peaks of BCS (λ_{max} = 221 and 331 nm), which confirmed that BBR and CGA were successfully assembled into a new complex unit. FT-IR spectroscopy was adopted to initially elucidate the binding sites for the self-assemblies (Fig. 1E). Compared to the stretching vibration of CGA from the carbonyl group at 1689 cm^{-1}, the IR absorption intensity from the corresponding carboxyl group band of BCS decreased. This could be attributed to the electrostatic interaction between the quaternary ammonium ion and carboxyl group during the self-assembly of BCS, which resulted in a low bond strength of BCS and reduced the frequency of the stretching vibration of the C=O double bond. In addition, fluorescence spectrophotometry was also used to determine the fluorescence properties of the self-assemblies. The optimal excitation wavelength of BBR, 350 nm, was used to determine the emission of the self-assembled products and their respective monomers. BBS exhibited a significant blueshift in the emission wavelength (CGA shifted from 432 to 425 nm and BBR shifted from 552 to 534 nm) (Fig. 1F), possibly because of the energy level difference between the excited state and the ground state as a result of self-assembly.

3.3. Self-assembly mechanism of the BCS

Additionally, ^{1}H NMR spectroscopy was carried out to examine the fundamental characteristics of self-assembly (Fig. 2A). The ^{1}H NMR spectra of BCS showed a supermolecular structure in which the banding ratio of BBR and CGA H signals was 2:1, illustrating the successful assembly of the BCS supermolecule from BBR and CGA. The chemical shifts of CGA H-8′, H-7′, and H-2′ clearly decreased from 6.15, 7.42, and 7.04 to 6.22, 7.44, and 7.06 ppm, respectively, following the production of the BCS supermolecule. These chemical shifts could be due to the π−π stacking of aromatic rings. Moreover, the chemical shifts of H-7 in CGA disappeared in the corresponding BCS, indicating the deprotonation of the carboxyl groups. Since the disappearance of the chemical shift peaks of H-3′ and H-4′ in BCS, we hypothesized that due to the special structure of BCS, the CGA was in the middle of the two-molecule BBR, which resulted in the shielding of these signals. In addition, the chemical shifts of H-8', H-3, and H-4 in CGA changed from 6.15, 5.07, and 3.57 to 6.22, 5.15, and 3.39 ppm, respectively (Fig. S3). Combined with the results of the FT-IR measurements, we inferred that the self-assembly process could be due to the electronic attraction of not only the carboxyl groups in CGA to the nitrogen atoms in BBR but also the active hydroxyl groups in CGA to the nitrogen atoms.

ITC analysis is a vital method for exploring the thermodynamic principle of interactions between BBR and CGA [34,35]. The binding energy of deionized water titrated with CGA was set as a benchmark, and the experimental group of prepared BCS was used to titrate CGA to BBR. Table S2 lists the energy change parameters of the interactions. Figs. 2B and C show the thermodynamic dimensions of the interactions between CGA and BBR. The association constant (K_a) of 5.43 × 10^4 indicated the stability of the self-assembly. The lower negative Gibbs energy change values (ΔG = −6.456 kcal/mol) indicated that the reaction between the two was a spontaneous exothermic process and was more likely to occur. With continual combination, the exothermicity of the peaks
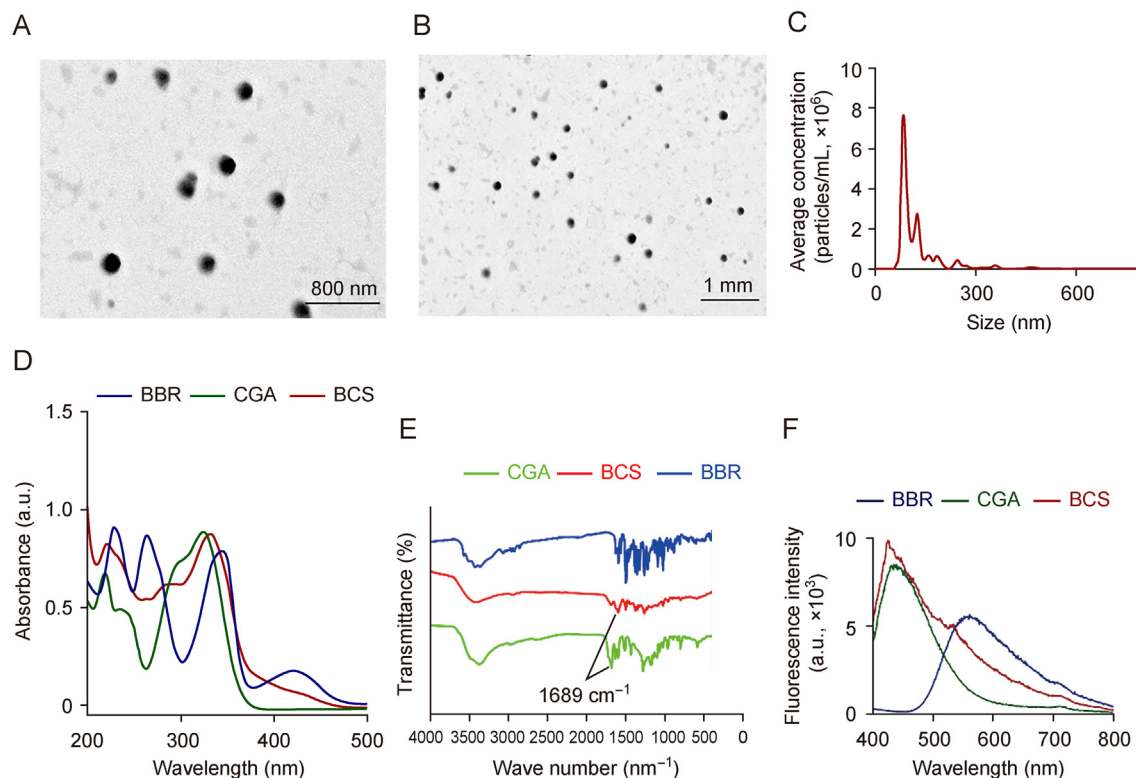
Fig. 1. Micromorphological properties and spectroscopic characterization of berberine (BBR)-chlorogenic acid (CGA) supramolecular (BCS), BBR, and CGA. (A, B) Transmission electron microscopy (TEM) images of BCS: BCS with scale bar of 500 nm (A) and 1 μm (B). (C) Size distribution of BCS determined by nanoparticle (NP) tracking analysis (NTA). (D) Ultraviolet-visible (UV-vis) absorption spectrograms of BCS, BBR, and CGA with a scan range from 200 to 500 nm. (E) Fourier transform-infrared (FT-IR) spectroscopy of BCS, BBR, and CGA with a scan range of 4000 to 400 cm^{-1}. (F) Fluorescence emission spectrum of BCS, BBR, and CGA with Ex = 350 nm and Em from 400 to 800 nm.

decreased, indicating an increasingly saturated process. Furthermore, the corresponding changes in the enthalpy ($\Delta H = -5.152$ kcal/mol, $-T\Delta S = -1.304$ kcal/mol) demonstrated that the assembly of BBR and CGA was an exothermic reaction driven by entropy-enthalpy. By fitting the titration curve, we found that the chemical binding ratio of CGA to BBR was approximately 0.6, which was similar to the previous result of the NMR hydrogen spectrum in which BBR and CGA were bound at a molar ratio of 2:1, and was also the favourable evidence for the self-assembly and binding of BBR and CGA. Additionally, a decrease in the homogeneity of the system energy was suggested by the negative ΔS (-1.304 kcal/mol), which may be related to the self-assembly of BCS. The formation of BCS is not a simple physical process; it involves intense chemical interactions driven by intermolecular hydrogen bonding, $\pi-\pi$ stacking, electrostatic interactions, and hydrophobic interactions.

Overall, BCS first formed a U-shaped one-dimensional (1D) planar structural unit by bridging the carboxyl group and the active hydroxyl group of CGA with the quaternary ammonium ion of BBR at a 2:1 ratio via electrostatic interactions. Then, driven by hydrophobic interactions and $\pi-\pi$ stacking, the U-shaped structural units were further assembled and stacked into 3D to form a large-scale amphiphilic sphere-like supramolecule composed of hydrophilic fragments outside and hydrophobic fragments inside (Fig. 2D). We also found sphere-like macromolecules formed by the RC-FM herbal pair in HLWMD with a series of assembly drivers and different $\pi-\pi$ stacking accumulation sites. Due to this tight assembly, amphiphilic BCS supramolecules were formed, allowing them to easily penetrate cell membranes. In addition, the 2:1 assembly ratio of the parent molecule increased the proportion of BBR in the overall BCS molecule. Zou et al. [36] and Wang et al. [37] showed that the hydrophobic methylene dioxy ring and free

methoxy group in BBR were important chemical structures for its anti-inflammatory effect, and the self-assembled BCS supramolecule contained more effective groups of BBR than did the free drug, which was the key to its anti-inflammatory effect. The self-assembly strategy of BBR and CGA provided a chemical basis for the compatibility theory of herbal pairs and the incompatibility theory of herbal prescriptions.

### 3.4. Estimation of sustained release and biocompatibility

The sustained release of BBR from BCS was examined in PBS. Fig. 3A displays that BBR quickly equilibrated during the first 2 h. While under common conditions, the release of BCS gradually increased over 24 h, and the release gradually reached equilibrium after 12 h, indicating that BCS was able to maintain slow and continuous release in vitro. To further evaluate the biocompatibility of self-assembling BCS, we first evaluated the haemolytic activities of BCS at concentrations ranging from 10 to 100 μM. As shown by the haemolysis results, there was no evident haemolysis of the RBCs in the rats after BCS treatment (Fig. 3B). Compared to the internationally accepted standard (5%), BCS has a lower rate of haemolysis, demonstrating its good biocompatibility. We also performed a CCK-8 test to assess the impact of different concentrations of BCS on cell viability. As shown in Figs. 3C and D, BCS and the corresponding free-drug dosage in the range of 10−80 μM had no apparent cytotoxic effects on cells at 24 or 48 h.

Moreover, we used fluorescence microscopy to preliminarily evaluate the cellular uptake of the BCS supramolecules. As shown in Fig. 3E, when cells were incubated with 10 μM FITC-labelled BCS supramolecules for different durations (3, 6, 9, and 12 h), the intracellular green fluorescence intensity increased in a time-dependent manner. When the incubation time reached 12 h, a significantly
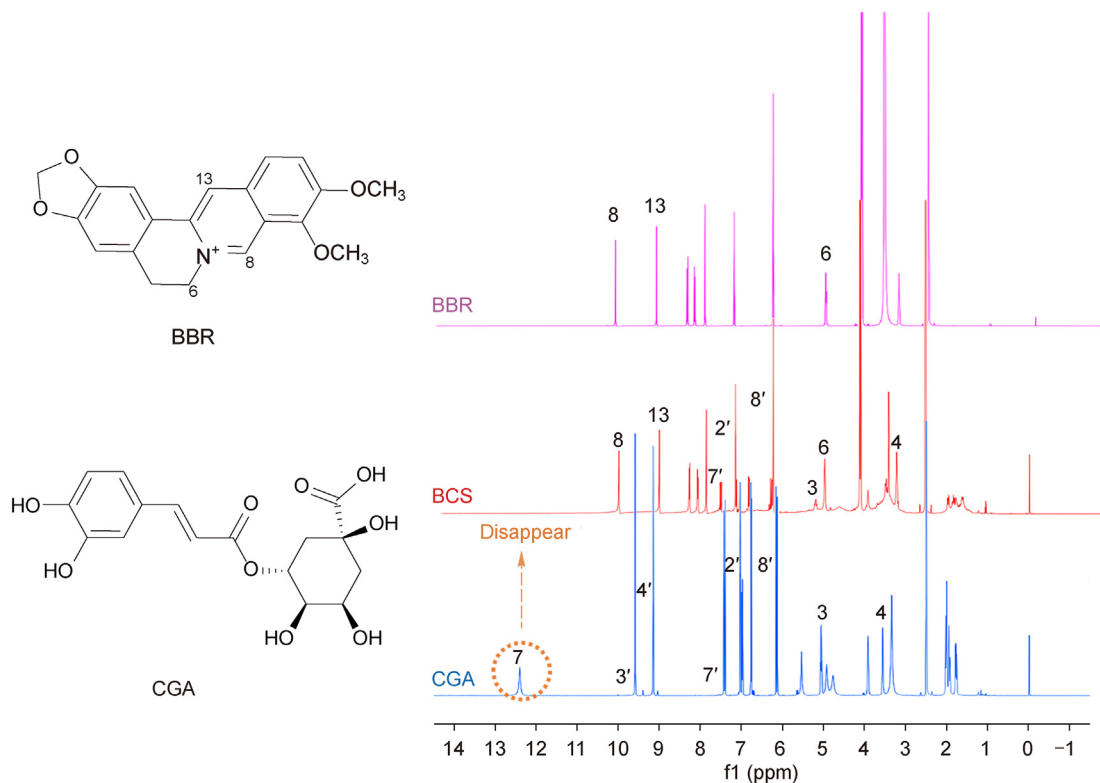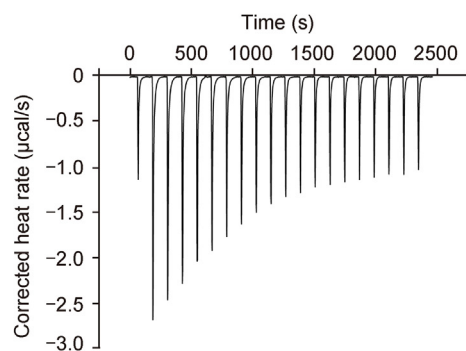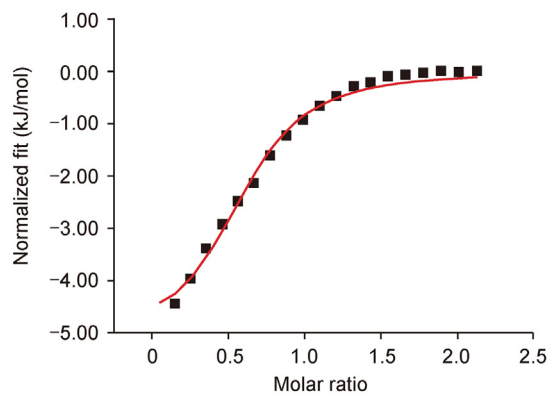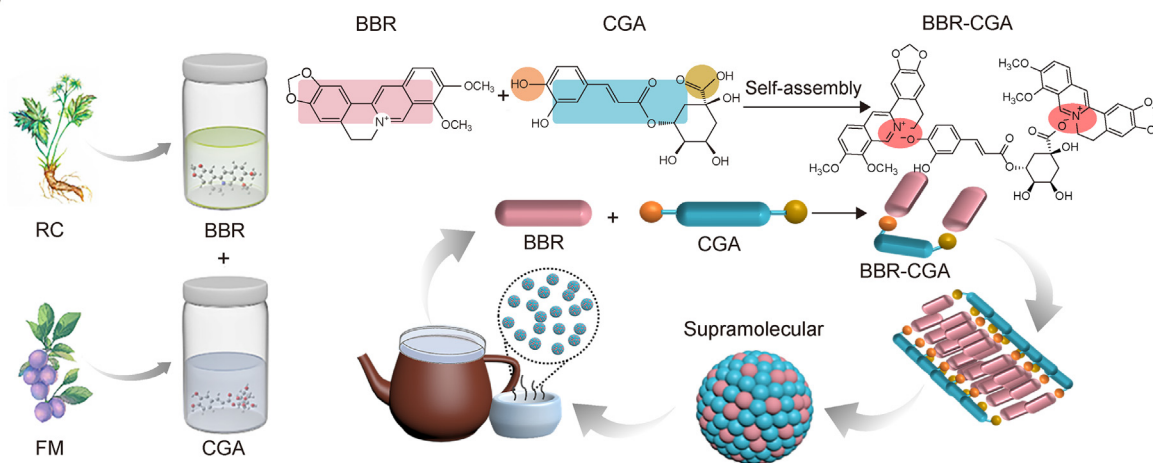
enhanced green fluorescence signal was observed. Compared with nuclei stained with DAPI, BCS could be efficiently taken up by cells into the cytoplasm (Fig. 3E), which may be closely related to its amphiphilic sphere-like molecular structure formed by self-assembly and was also the chemical basis for its improved pharmacological effects.

3.5. BCS exhibits better anti-inflammatory effects

For clinical transformation, we utilized the LPS-induced RAW264.7 cell line to explore the anti-inflammation impact of BCS. Intracellular ROS are regarded as core factors that amplify inflammation and trigger inflammatory responses [38]. RAW264.7 cells were observed by a laser scanning confocal microscope to directly visualize the intracellular localization of ROS after LPS stimulation (Fig. 4A). The green fluorescence intensity of the LPS-treated cells was noticeably greater than that of the cells in the control group, indicating an increase in intracellular ROS levels. However, this effect was reversed by treatment with the free drugs and BCS, and this result revealed that BCS exhibited better inflammatory prevention than the free drug. As shown in Fig. 4B, LPS induced significant ROS generation by 1.2-fold compared with that in the control group. After pretreatment with different concentrations of BBR, CGA, or BCS (10−100 μM), the ROS levels decreased in a dose-dependent manner. BBS exhibited better anti-inflammatory effects. Treatment of macrophages with the lowest concentration of BCS (10 μM) dramatically inhibited the generation of ROS induced by LPS, with an inhibition rate of approximately 60% (Fig. 4B). Therefore, we chose the lowest concentration of free drugs and BCS (10 μM) to treat the cells in subsequent cell experiments.

During LPS-induced inflammation, pattern recognition receptors (PRRs), including Toll-like receptors (TLRs), PAMPs, and DAMPs, which are expressed on the surface or inside macrophages, can respond rapidly to further activate NF-κB and other signalling molecules [39], leading to the release of a series of inflammatory mediators and cytokines, including tumour necrosis factor alpha (TNF-α), IL-1β, IL-18, and inducible NO synthase (iNOS) [40]. Among them, TNF-α can promote the production of iNOS in immune cells, which plays an important regulatory role in the immune system. As shown in Figs. 4C−E, after being induced by LPS (1 μg/mL), we found a significant increase in the contents of IL-1β, IL-18, and NO in the supernatant compared with those before. BBR, CGA, and BCS treatment significantly inhibited the overexpression of each cytokine in the supernatant of macrophages ($P < 0.0001$). Moreover, BCS showed better anti-inflammatory effects than the free drugs.

Based on the aforementioned findings, we inferred that BBR and CGA self-assemble into amphiphilic supramolecular BCSs, which can easily penetrate the cell membrane, effectively enter the cytoplasm, and continuously and stably release active components to exert their pharmacological effects. In addition, due to the special structure (hydrophilic fragments outside and hydrophobic fragments inside) and ratio of BCS (CGA:BBR = 1:2), compared with free drugs, BCS can markedly decrease the generation of ROS and the expression of proinflammatory cytokines, resulting in better anti-inflammatory effects.

3.6. BCS exerts its anti-inflammatory effects mainly by inhibiting pyroptosis in macrophages

In the LPS-induced cell inflammation model, we observed under a microscope that the morphology of cells treated with LPS became indistinct, with some cells exhibiting swelling and rupture, which are characteristic of pyroptosis. To further confirm whether pyroptosis occurred in RAW264.7 cells after LPS treatment, we used PI staining and scanning electron microscopy (SEM) to observe cell morphology. Following LPS stimulation, the cells exhibited pronounced lytic death (Fig. 5A), whereas cellular damage in the BCS-treated group was comparatively minor. SEM revealed that control cells were round-like cell clusters (Fig. 5B), but LPS-treated cells had irregular margins, most typically characterized by the presence of membrane pits and pores of different sizes in the cytoplasmic membrane and rounded vesicle-like exudation of cell contents, which is also a typical cell morphology of pyroptosis (Fig. 5B). BCS treatment significantly alleviated pore formation and exudation on the cell surface. The quantitative results of PI-stained lytic dead cells were shown in Fig. 5C, and a LDH release assay was used to further evaluate the viability of pyroptotic cells. Compared with that in the control group, the release of LDH dramatically increased ($P < 0.0001$, Fig. 5D). Notably, BCS treatment alone did not induce LDH release, cell lysis, or death. However, in the presence of LPS, 10 μM BCS significantly inhibited these processes ($P < 0.0001$), demonstrating enhanced inhibitory effects on lytic death compared to either agent alone (BBR or CGA).

3.7. BCS further inhibited the NF-κB- and caspase 11-mediated noncanonical proptosis signalling pathways in macrophages

The macrophage response to inflammation involves two principal stages. The initial stage is characterized by a swift response through PRRs on the cell surface or intracellularly, activating signalling molecules such as NF-κB, which in turn triggers the release of inflammatory regulators and cytokines, such as TNF-α, IL-1β, IL-18, and iNOS [40]. This is followed by the activation stage, wherein various inflammasomes respond to diverse PAMPs and DAMPs within macrophages, resulting in the transcriptional upregulation of inflammasome constituents such as caspase-4/5/11, caspase-1, and NLRP3, thereby further inducing pyroptosis [41,42]. Our findings indicated that the anti-inflammatory effect of BCS was closely associated with the inhibition of pyroptosis. To elucidate the key genes and specific mechanisms by which BCS inhibits pyroptosis, total RNA was extracted from the aforementioned treatment groups for RNA-seq analysis. We concentrated on the genes that exhibited callback after BCS treatment and constructed three transcriptome libraries (from the control, model, and BCS-treated groups). A circular diagram of differential gene enrichment (Fig. 6A) revealed that BCS predominantly regulated genes associated with cellular organismal systems, with approximately 219 DEGs identified. KEGG pathway analysis was performed for the above target genes, and a total of 15 KEGG pathways were significantly enriched (Fig. 6B). According to the KEGG enrichment analysis results, BCS observably regulated the NOD-like signalling pathway. The NOD-like signalling pathway is a crucial cellular signalling pathway that plays a significant role in the innate immune response. This pathway is activated upon the recognition of PAMPs, such as LPS. The expression of inflammasome components, including caspase-4/5/11, caspase-1, and NLRP3, was upregulated in macrophages after stimulation with PAMPs. These cascades further promote the release of proinflammatory factors, including IL-1β and IL-18, thereby inducing a lytic form of cell death known as pyroptosis [13,43]. Consequently, based on the literature and RNA-seq data, we hypothesized that BCS mediates its anti-inflammatory effects through the modulation

Fig. 2. Characterization of the self-assembly mechanism of berberine (BBR)-chlorogenic acid (CGA) supramolecular (BCS). (A) 500 MHz ^{1}H nuclear magnetic resonance (NMR) spectrum of BBR, CGA, and BCS in dimethyl sulfoxide (DMSO)-d6 solution. (B, C) The corrected data of isothermal titration calorimetry (ITC) (B) and fitting curves (C), including the thermodynamic parameters of BBR-CGA titration. (D) Illustration of the self-assembly mechanism and stability of BCS. RC: *Rhizoma Coptidis*; FM: *Fructus Mume*.
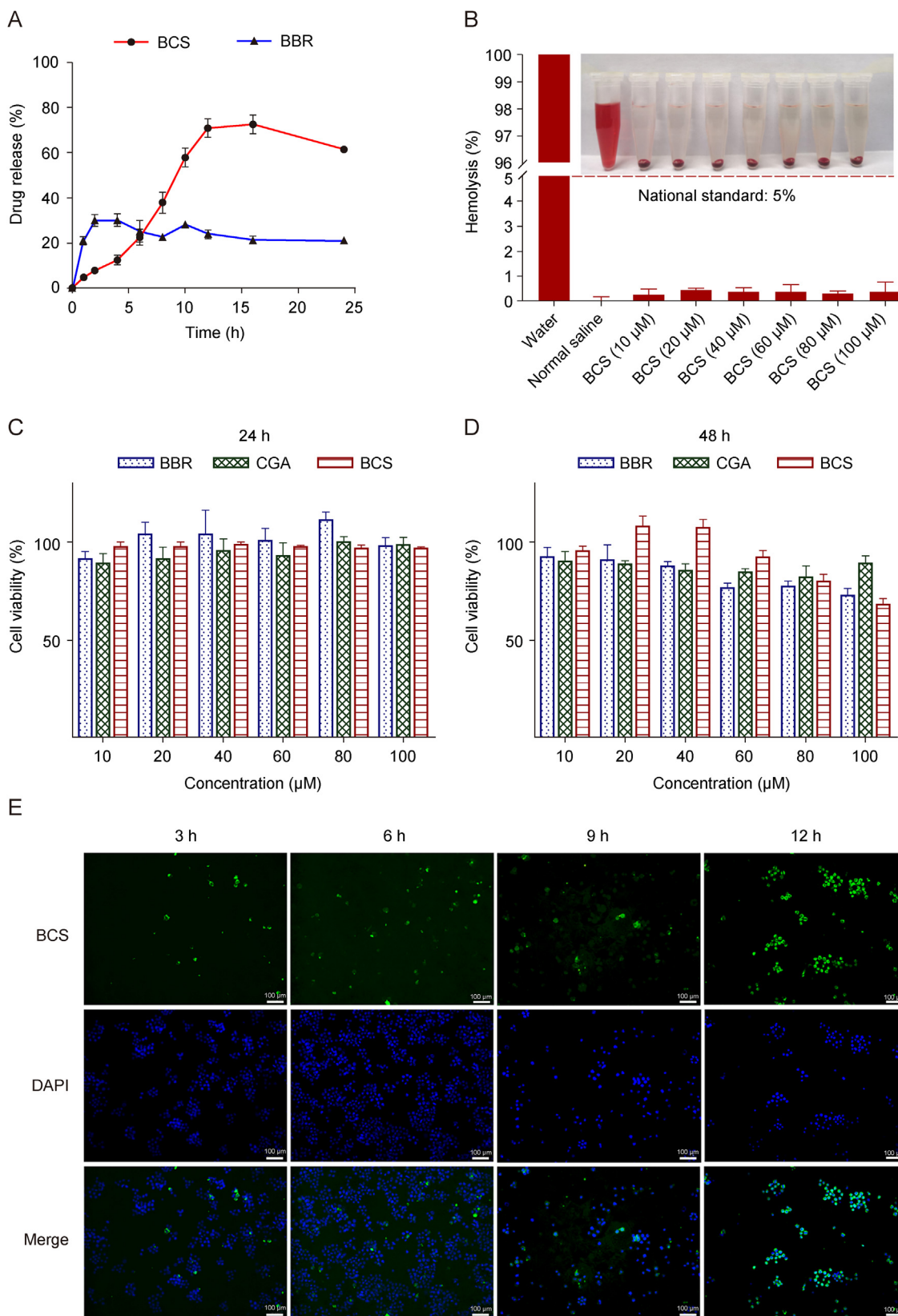
Fig. 3. Evaluation of the cellular uptake and biocompatibility of berberine (BBR)-chlorogenic acid (CGA) supramolecular (BCS). (A) Drug release profile of BCS and BBR. (B) Hemolytic activities of BCS ranging from 10 to 100 µM. *In-vitro* biosecurity characterization of BCS, BBR, and CGA. Inset shows photographs of corresponding solutions after blood centri-fugation. (C, D). *In-vitro* cell viability assays of BCS, BBR, and CGA after 24 h (C) and 48 h (D). (E) Fluorescence images of celluar uptake of fluorescein isothiocyanate (FITC)-labelled BCS (10 µM) after treatment at various time intervals (3, 6, 9, and 12 h). DAPI: 4′,6-diamidino-2-phenylindole.
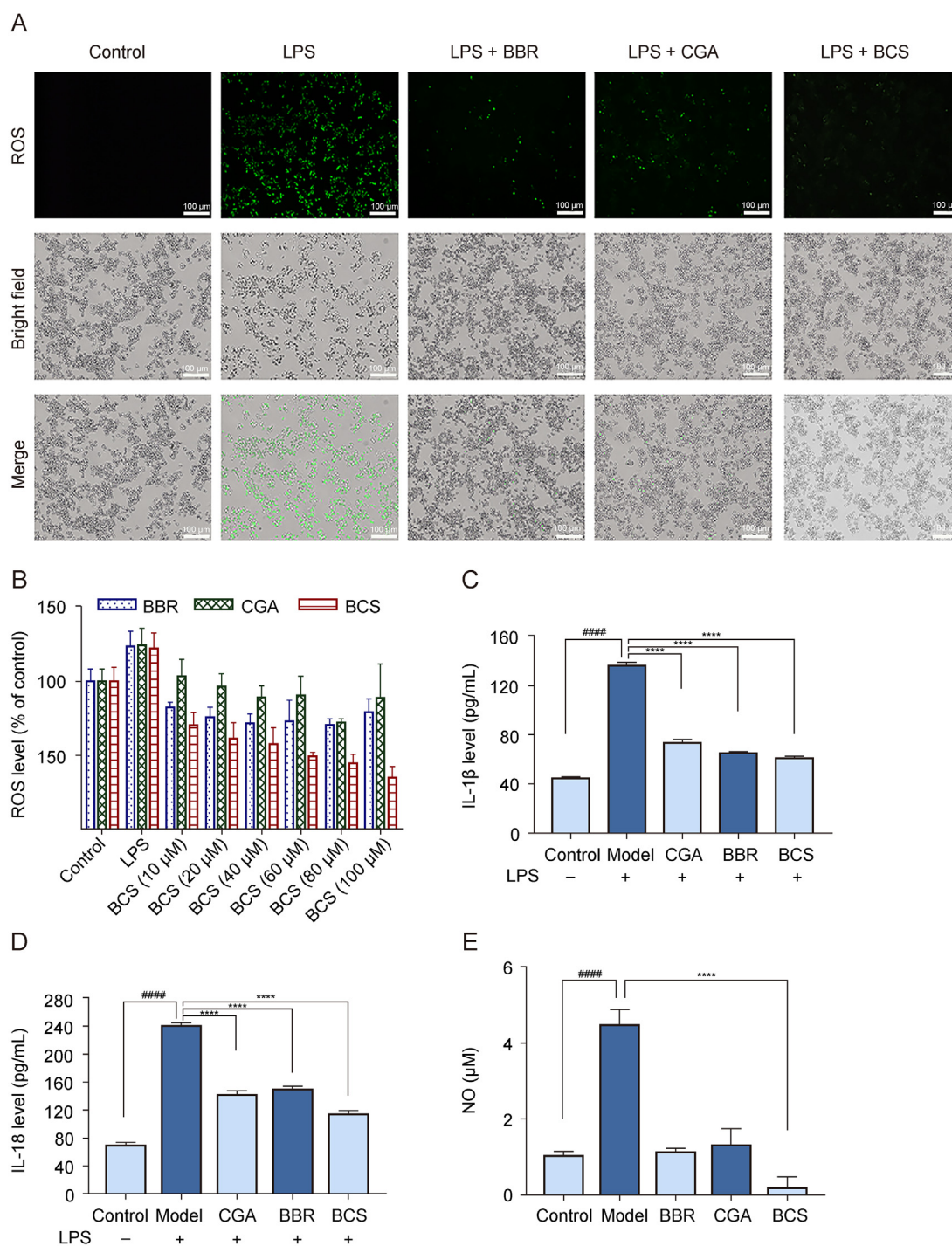
Fig. 4. Investigation of the anti-inflammatory properties of berberine (BBR)-chlorogenic acid (CGA) supramolecular (BCS). (A) Fluorescence imaging of intracellular reactive oxygen species (ROS) with BCS, BBR, and CGA at 10 μM. (B) Quantitative assessment of intracellular ROS levels following treatment with varying concentrations of BBR, CGA, BCS, and control, with or without lipopolysaccharide (LPS) induction (1 μg/mL). (C, D) Enzyme-linked immunosorbent assay (ELISA) measurements of interleukin-1β (IL-1β) (C) and IL-18 (D) secretions into the cell culture media. (E) Nitric oxide (NO) levels were determined by Griess assay. All data are expressed as means ± standard deviation (SD). Statistical differences were analyzed using one-way analysis of variance (ANOVA). $^{####}P < 0.0001$, compared with the control group; $^{****}P < 0.0001$, compared with the LPS-induced model group.

of relevant signalling pathways and the mitigation of inflammasome-induced pyroptosis.

Transcriptomic analysis of BCS-treated RAW264.7 cells revealed 21 genes significantly enriched in the NOD signalling pathway compared to those in the LPS-stimulated group. Notably, the expression of caspase-11 was markedly reduced (Fig. 6C). Recent research indicates that LPS directly triggers the activation of

caspase-4/5/11, initiating the atypical inflammasome pathway and subsequently leading to the activation of caspase-1 and the maturation of IL-1β via the classical inflammasome pathway. Both caspase-1 and caspase-11 cleave gasdermin D (GSDMD) to produce an N-terminal fragment (GSDMD-NT) to form pores in the plasma membrane, which facilitates pyroptosis [44,45]. BCS substantially downregulated the gene expression of caspase-11 by nearly
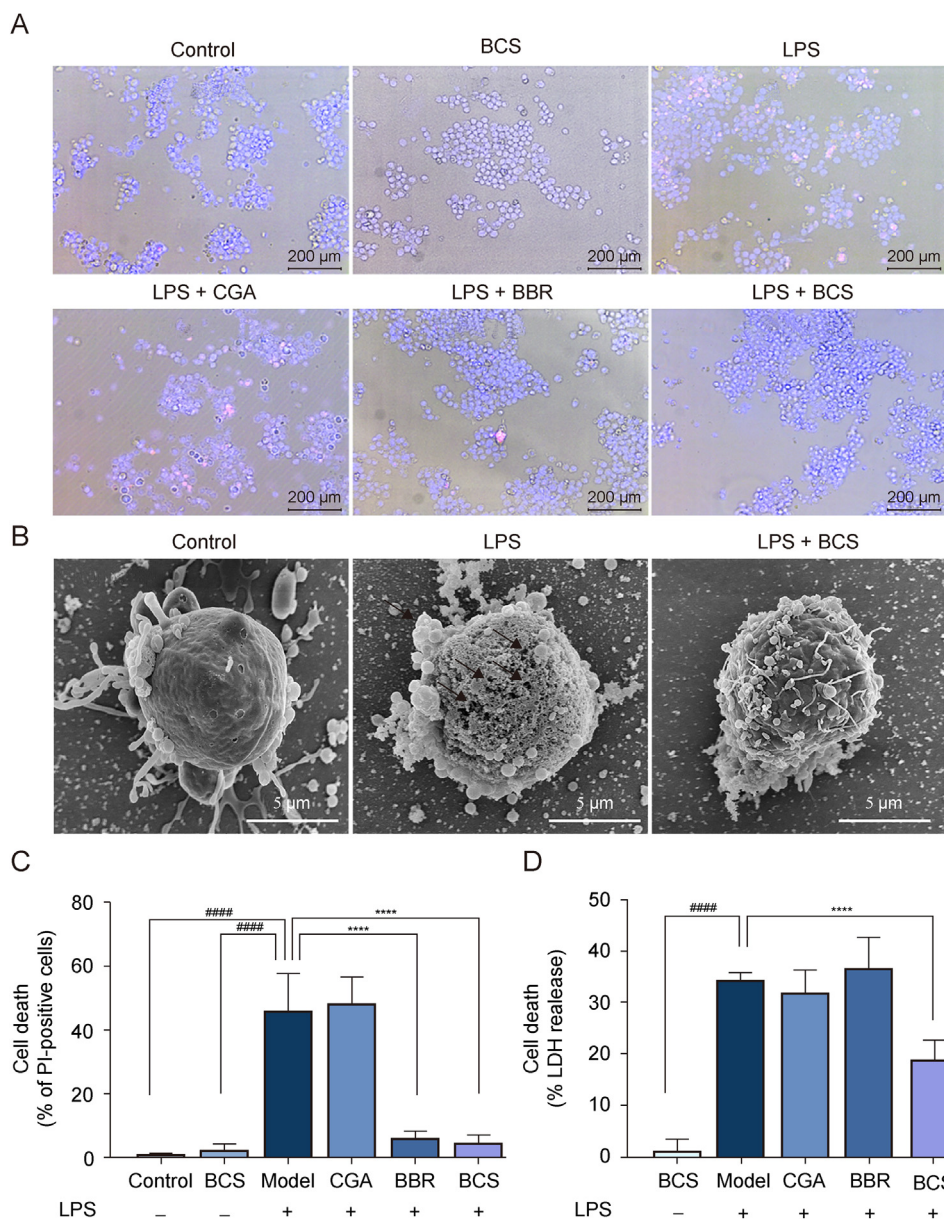
Fig. 5. Anti-inflammatory effect of berberine (BBR)-chlorogenic acid (CGA) supramolecular (BCS) mediated through the inhibition of cell pyroptosis. (A) The death of pyroptotic cells were detected by propidium iodide (PI) staining (red) and visualized in conjunction with Hoechst 33342 (blue). (B) Scanning electron micrographs (SEM) of RAW264.7 cells post-treatment with lipopolysaccharide (LPS) (1 μg/mL) and/or BCS (10 μM) for 24 h. (C) Quantification of PI-positive cells using ImageJ software from five random fields, and the percentage of cell death was calculated as the ratio of PI-positive cells to all cells (labelled by Hoechst 33342). (D) Lactic acid dehydrogenase (LDH) release as an indicator of cell death. Data are expressed as mean ± standard deviation (SD) and analyzed using one-way analysis of variance (ANOVA). $^{####}P < 0.0001$, compared with the control group; $^{****}P < 0.0001$, compared with the LPS-induced model group.

threefold compared with that in the LPS group. Given that the inflammatory response of macrophages typically proceeds in two steps, we confirmed the expression of genes and inflammatory factors related to pyroptosis in BCS-treated RAW264.7 cells using qRT-PCR. NF-κB, a crucial cytoplasmic nuclear transcription factor, is translocated to the nucleus upon LPS-induced activation to regulate the transcription of proinflammatory mediators [46]. After the activation of NF-κB, BCS notably suppressed the release of inflammatory factors including TNF-α, IL-6, and iNOS, as depicted in Figs. 6D–F. Furthermore, BCS attenuated the mRNA expression of caspase-11 in the noncanonical inflammasome pathway, diminishing the mRNA levels of caspase-1, NLRP3, IL-1β, and IL-18 in the canonical pathway, thereby mitigating the release of inflammatory

factors and exerting an anti-inflammatory effect (Figs. 6G–K). This anti-inflammatory effect of BCS surpassed that of the free drug, consistent with previous experimental results. Western blot analysis confirmed the anti-inflammatory effects of BCS, revealing a significant decrease in the phosphorylation of NF-κB p65 stimulated by LPS and a subsequent decrease in the protein level of caspase-11 (Fig. 7A). Semiquantitative data also confirmed that BCS substantially reduced the LPS-induced increase in the p-p65/p65 ratio and the relative expression of the above proteins (Figs. 7B and C). Collectively, our findings demonstrated that BCS, a self-assembled supramolecule from the herbal pair of HL-WM, formed amphiphilic spherical structures through electrostatic interactions, π−π stacking, and hydrophobic interactions between BBR and CGA.
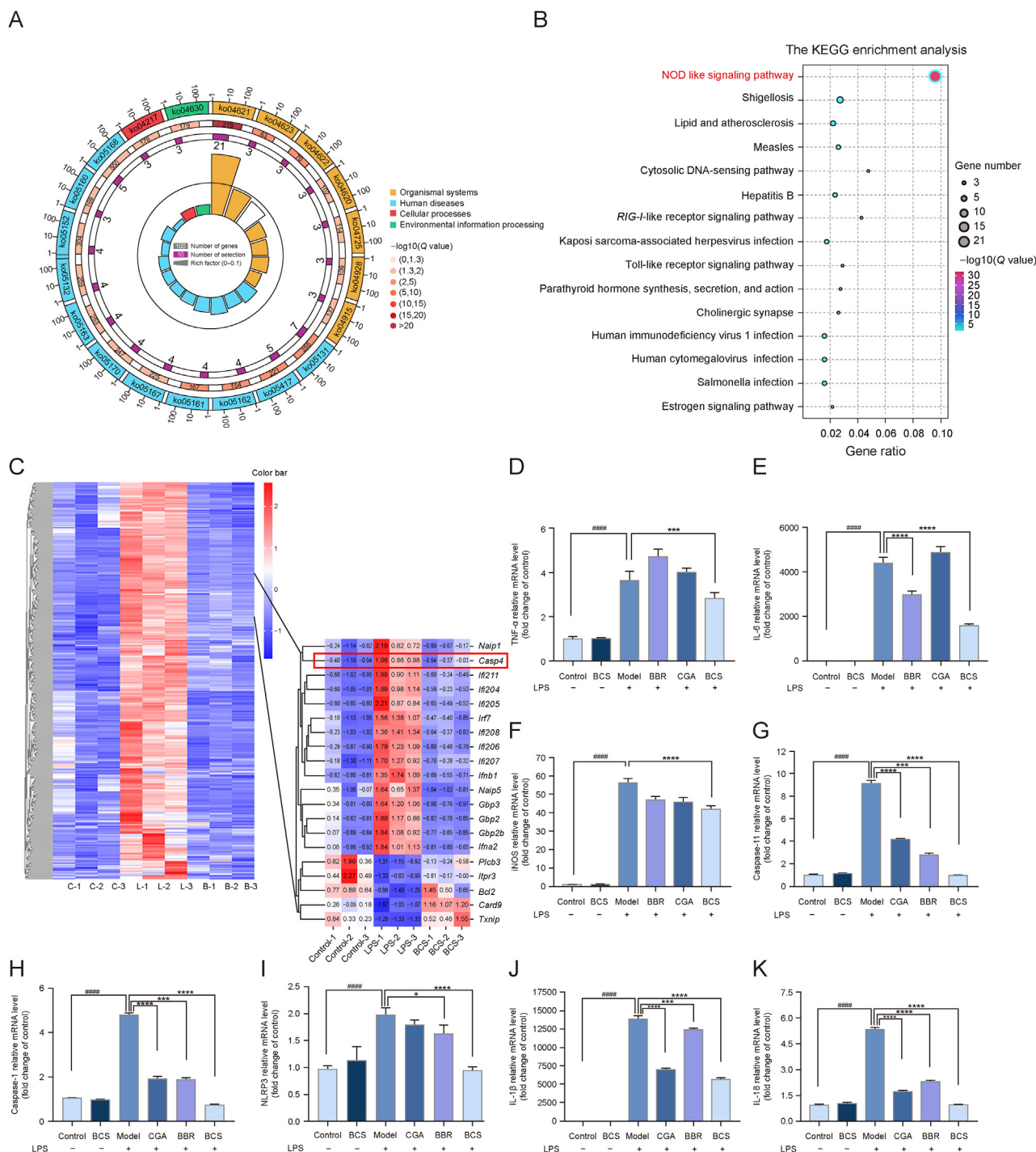
Fig. 6. BCS modulation of nuclear factor-kappaB (NF-κB) and caspase-4/5/11-regulated non-canonical proptosis pathways in RAW264.7 cells. (A) Differential gene expression and functional annotations induced by berberine (BBR)-chlorogenic acid (CGA) supramolecular (BCS) were represented by enrichment circle plots. (B) Top15 Kyoto Encyclopedia of Genes and Genomes (KEGG) enrichment analysis shown in a scatterplot. (C) Heatmap representation of microarray analysis in control, lipopolysaccharide (LPS)-induced model (1 μg/mL), and BCS-treated RAW264.7 cells (10 μM), with three biological replicates per group. (D–K) Real-time polymerase chain reaction (PCR) assay of messenger RNA (mRNA) levels for tumor necrosis factor alpha (TNF-α) (D), interleukin-6 (IL-6) (E), inducible nitric oxide (NO) synthase (iNOS) (F), caspase 11 (G), caspase-1 (H), nucleotide-binding oligomerization domain (NOD)-like receptor family pyrin domain-containing 3 (NLPR3) (I), IL-1β (J), and IL-18 (K), respectively. Data are expressed as means ± standard deviation (SD) and analyzed using one-way analysis of variance (ANOVA). $^{####}P < 0.0001$, compared with the control group; $^{*}P < 0.05$, $^{***}P < 0.001$, and $^{****}P < 0.0001$, compared with the LPS-induced model group. *RIG-I*: retinoic acid-inducible gene I.

This structural arrangement enhanced the anti-inflammatory effects of BCS over those of the free drug. The anti-inflammatory effects of BCSs are intricately linked to the inhibition of pyroptosis. RNA-seq and Western blot analyses have elucidated the dual mode of action of BCS: attenuating inflammatory factor release by inhibiting NF-κB p65 phosphorylation and suppressing the caspase-11-mediated noncanonical pathway. These findings suggest a potential mechanism by which BCS exerts anti-inflammatory effects and offer a novel approach to understanding multidrug combinations in TCM.
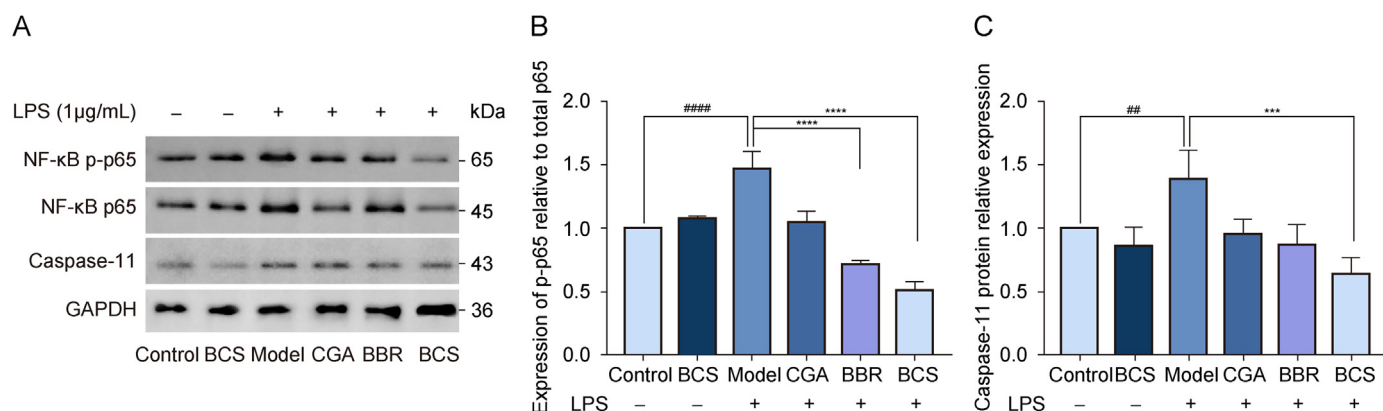
Fig. 7. Downregulation of the nuclear factor-kappaB (NF-κB) and caspase-4/5/11-associated protein expression by berberine (BBR)-chlorogenic acid (CGA) supramolecular (BCS) in the noncanonical pyroptosis pathway. (A) Western blot analysis of protein levels in cell lysates, with glyceraldehyde-3-phosphate dehydrogenase (GAPDH) serving as a loading control. (B) Quantitative evaluation of relative NF-κB p65 phosphorylation levels. (C) Normalized caspase-11 expression relative to the control group. Data are expressed as mean ± standard deviation (SD) and analyzed using one-way analysis of variance (ANOVA). $^{\#\#}P < 0.01$ and $^{\#\#\#\#}P < 0.0001$, compared with the control group; $^{***}P < 0.001$, and $^{****}P < 0.0001$, compared with the lipopolysaccharide (LPS)-induced model group.

4. Conclusion

Collectively, inspired by the theory of natural product compatibility, we successfully obtained the supramolecular structural unit BCS formed by the self-assembly of its main components, BBR and CGA, using the classical herbal pair RC-FM as an example. A series of characterization methods were adopted to confirm the self-assembly mechanism of BCS. BCS first forms a U-shaped 1D planar structural unit by bridging the carboxyl group and the active hydroxyl group of CGA with the quaternary ammonium ion of BBR at a 1:2 molar ratio via electrostatic interactions. Then, driven by π−π stacking and hydrophobic interactions, the U-shaped structural units were further assembled and stacked into three dimensions to form a large-scale amphiphilic sphere-like supramolecule: hydrophilic fragments outside and hydrophobic fragments inside. This stacking pattern and the amphiphilic molecular structure of BCS significantly improved its antibacterial performance compared with that of single free molecules. Compared with single free drugs, BCS supramolecules can more easily penetrate cell membranes and can significantly suppress the generation of ROS and the release of inflammatory regulators (such as NO, IL-1β, and IL-18) induced by LPS. Further fluorescence staining analysis revealed that the anti-inflammatory effect of BCS was closely associated with the inhibition of pyroptosis. To further investigate the molecular mechanism by which BCS inhibits pyroptosis to alleviate inflammatory diseases, RNA-seq, qRT-PCR, and Western blotting were used. BCS, which has amphiphilic fluoric properties, could easily cross the cell membrane and play a better anti-inflammatory role by inhibiting the phosphorylation of NF-κB p65 and inhibiting the caspase-4/5/11-regulated noncanonical pyroptosis pathway. The self-assembled amphiphilic supramolecular structure obtained by drug pairing was the key to enhancing the anti-inflammatory effect. Our findings explained the scientific connotation of drug compatibility from the perspective of self-assembly of TCM and put forwards a new idea to understand the synergistic anti-inflammatory effect of *the* RC-FM pair, which also provided a new strategy for elucidating the mechanism of multi-herb combinations.

CRediT authorship contribution statement

Wenhui Qian: Writing − review & editing, Writing − original draft, Data curation. **Bei Zhang:** Writing − original draft, Software, Methodology, Investigation, Data curation, Conceptualization. **Ming Gao:** Investigation. **Yuting Wang:** Visualization, Investigation, Data curation. **Jiachen Shen:** Software, Investigation. **Dongbing Liang:** Formal analysis, Data curation. **Chao Wang:** Validation, Investigation. **Wei Wei:** Data curation. **Xing Pan:** Software, Data curation. **Qiuying Yan:** Validation, Investigation. **Dongdong Sun:** Supervision, Funding acquisition. **Dong Zhu:** Writing − review & editing, Supervision, Resources, Funding acquisition, Conceptualization. **Haibo Cheng:** Supervision, Resources.

Declaration of competing interest

The authors declare that there are no conflicts of interest.

Acknowledgments

Appendix A. Supplementary data

Supplementary data to this article can be found online at https://doi.org/10.1016/j.jpha.2024.101056.

References

[1] H.-C. Ku, S.-Y. Lee, S.-S. Lee, et al., Thaliporphine, an alkaloid from Neolitsea konishii, exerts antioxidant, anti-inflammatory, and anti-apoptotic responses in guinea pig during cardiovascular collapse in inflammatory disease, J. Funct. Foods 26 (2016) 57−64.
[2] C.-J. Liou, S. Wu, L. Chen, et al., Acacetin from traditionally used *Saussurea involucrata* Kar. et kir. suppressed adipogenesis in 3T3-L1 adipocytes and attenuated lipid accumulation in obese mice, Front. Pharmacol. 8 (2017), 589.
[3] D. Hirayama, T. Iida, H. Nakase, The phagocytic function of macrophage-enforcing innate immunity and tissue homeostasis, Int. J. Mol. Sci. 19 (2017), 92.
[4] M. Wu, J. Lu, Autophagy and macrophage functions: Inflammatory response and phagocytosis, Cells 9 (2019), 70.
[5] M. Biasizzo, N. Kopitar-Jerala, Interplay between NLRP3 inflammasome and autophagy, Front. Immunol. 11 (2020), 591803.
[6] E.-K. Jo, J.K. Kim, D.-M. Shin, et al., Molecular mechanisms regulating NLRP3 inflammasome activation, Cell. Mol. Immunol. 13 (2016) 148−159.

[7] M. Groslambert, B.F. Py, Spotlight on the NLRP3 inflammasome pathway, J. Inflamm. Res. 11 (2018) 359−374.

[8] S. Paik, J.K. Kim, P. Silwal, et al., An update on the regulatory mechanisms of NLRP3 inflammasome activation, Cell. Mol. Immunol. 18 (2021) 1141−1160.

[9] Z. Wang, W. Hu, C. Lu, et al., Targeting NLRP3 (nucleotide-binding domain, leucine-rich-containing family, pyrin domain-containing-3) inflammasome in cardiovascular disorders, Arterioscler. Thromb. Vasc. Biol. 38 (2018) 2765−2779.

[10] R. Fusco, R. Siracusa, T. Genovese, et al., Focus on the role of NLRP3 inflammasome in diseases, Int. J. Mol. Sci. 21 (2020), 4223.

[11] S. Wang, Y. Yuan, N. Chen, et al., The mechanisms of NLRP3 inflammasome/pyroptosis activation and their role in Parkinson's disease, Int. Immunopharmacol. 67 (2019) 458−464.

[12] P. Yu, X. Zhang, N. Liu, et al., Pyroptosis: Mechanisms and diseases, Signal Transduct. Target. Ther. 6 (2021), 128.

[13] X. Huang, Y. Feng, G. Xiong, et al., Caspase-11, a specific sensor for intracellular lipopolysaccharide recognition, mediates the non-canonical inflammatory pathway of pyroptosis, Cell Biosci. 9 (2019), 31.

[14] L. Wang, W. Wei, X. Zhang, et al., An integrated proteomics and bioinformatics approach reveals the anti-inflammatory mechanism of carnosic acid, Front. Pharmacol. 9 (2018), 370.

[15] M. Mosihuzzaman, Herbal medicine in healthcare − An overview, Nat. Prod. Commun. 7 (2012) 807−812.

[16] X. Zhou, S.W. Seto, D. Chang, et al., Synergistic effects of Chinese herbal medicine: A comprehensive review of methodology and current research, Front. Pharmacol. 7 (2016), 201.

[17] J. Wang, A. Sasse, H. Sheridan, Traditional Chinese medicine: From aqueous extracts to therapeutic formulae. Plant Extracts, IntechOpen Limited, London, 2019.

[18] T.-P. Fan, Y. Zhu, C. Leon, et al., Traditional Chinese medicine herbal drugs: From heritage to future developments. The Science and Regulations of Naturally Derived Complex Drugs. Springer, Cham, 2019, pp. 59−77.

[19] S. Wang, Y. Hu, W. Tan, et al., Compatibility art of traditional Chinese medicine: From the perspective of herb pairs, J. Ethnopharmacol. 143 (2012) 412−423.

[20] X.H. Ma, C.J. Zheng, L.Y. Han, et al., Synergistic therapeutic actions of herbal ingredients and their mechanisms from molecular interaction and network perspectives, Drug Discov. Today 14 (2009) 579−588.

[21] X. Wu, H. Chen, X. Gao, et al., Natural herbal remedy Wumei decoction ameliorates intestinal mucosal inflammation by inhibiting Th1/Th17 cell differentiation and maintaining microbial homeostasis, Inflamm Bowel Dis. 28 (2022) 1061−1071.

[22] Y. Yang, G. Xiao, P. Cheng, et al., Protective application of Chinese herbal compounds and formulae in intestinal inflammation in humans and animals, Molecules 28 (2023), 6811.

[23] S. Yan, P. Wang, H. Wei, et al., Treatment of ulcerative colitis with Wu-Mei-Wan by inhibiting intestinal inflammatory response and repairing damaged intestinal mucosa, Phytomedicine 105 (2022), 154362.

[24] F. Meng, Z. Wu, Z. Yin, et al., Coptidis rhizoma and its main bioactive components: Recent advances in chemical investigation, quality evaluation and pharmacological activity, Chin. Med. 13 (2018), 13.

[25] X. Shang, H. Pan, M. Li, et al., *Lonicera japonica* Thunb.: Ethnopharmacology, phytochemistry and pharmacology of an important traditional Chinese medicine, J. Ethnopharmacol. 138 (2011) 1−21.

[26] C. Bailly, Anticancer properties of *Prunus mume* extracts (Chinese plum, Japanese apricot), J. Ethnopharmacol. 246 (2020), 112215.

[27] F. Wu, Q. Shao, Z. Cheng, et al., Traditional herbal formula Wu-Mei-Wan alleviates TNBS-induced colitis in mice by inhibiting necroptosis through increasing RIPK3 O-GlcNAcylation, Chin. Med. 16 (2021), 78.

[28] S. Zhang, Discovery and design of self-assembling peptides, Interface Focus 7 (2017), 20170028.

[29] A.R. Hirst, B. Escuder, J.F. Miravet, et al., High-tech applications of self-assembling supramolecular nanostructured gel-phase materials: From regenerative medicine to electronic devices, Angew. Chem. Int. Ed. Engl. 47 (2008) 8002−8018.

[30] S. Li, T. Xiao, C. Lin, et al., Advanced supramolecular polymers constructed by orthogonal self-assembly, Chem. Soc. Rev. 41 (2012) 5950−5968.

[31] J.M. Zayed, N. Nouvel, U. Rauwald, et al., Chemical complexity − Supramolecular self-assembly of synthetic and biological building blocks in water, Chem. Soc. Rev. 39 (2010) 2806−2816.

[32] Z. Wang, J. Lu, Z. Yuan, et al., Natural carrier-free binary small molecule self assembled hydrogel synergize antibacterial effects and promotewound healing by inhibiting virulence factors and alleviating the inflammatory response, Small 19 (2023), e2205528.

[33] P. Liang, T. Bi, Y. Zhou, et al., Insights into the mechanism of supramolecular self-assembly in the *Astragalus membranaceus-Angelica sinensis* codecoction, ACS Appl. Mater. Interfaces. 15 (2023) 47939−47954.

[34] R. Huang, B.L.T. Lau, Biomolecule-nanoparticle interactions: Elucidation of the thermodynamics by isothermal titration calorimetry, Biochim. Biophys. Acta 1860 (2016) 945−956.

[35] M. Kabiri, L.D. Unsworth, Application of isothermal titration calorimetry for characterizing thermodynamic parameters of biomolecular interactions: Peptide self-assembly and protein adsorption case studies, Biomacromolecules 15 (2014) 3463−3473.

[36] K. Zou, Z. Li, Y. Zhang, et al., Advances in the study of berberine and its derivatives: A focus on anti-inflammatory and anti-tumor effects in the digestive system, Acta Pharmacol. Sin. 38 (2017) 157−167.

[37] B. Wang, A. Deng, Z. Li, et al., Syntheses and structure-activity relationships in growth inhibition activity against human cancer cell lines of 12 substituted berberine derivatives, Molecules 25 (2020), 1871.

[38] J. Checa, J.M. Aran, Reactive oxygen species: Drivers of physiological and pathological processes, J. Inflamm. Res. 13 (2020) 1057−1073.

[39] X. Wang, V. Antony, Y. Wang, et al., Pattern recognition receptor-mediated inflammation in diabetic vascular complications, Med. Res. Rev. 40 (2020) 2466−2484.

[40] H. Duez, B. Pourcet, Nuclear receptors in the control of the NLRP3 inflammasome pathway, Front. Endocrinol. 12 (2021), 630536.

[41] A. Zamyatina, H. Heine, Lipopolysaccharide recognition in the crossroads of TLR4 and caspase-4/11 mediated inflammatory pathways, Front. Immunol. 11 (2020), 585146.

[42] Y.-S. Yi, Caspase-11 non-canonical inflammasome: A critical sensor of intracellular lipopolysaccharide in macrophage-mediated inflammatory responses, Immunology 152 (2017) 207−217.

[43] A. Abu Khweek, A.O. Amer, Pyroptotic and non-pyroptotic effector functions of caspase-11, Immunol. Rev. 297 (2020) 39−52.

[44] X. Liu, Z. Zhang, J. Ruan, et al., Inflammasome-activated gasdermin D causes pyroptosis by forming membrane pores, Nature 535 (2016) 153−158.

[45] X. Liu, J. Lieberman, A mechanistic understanding of pyroptosis: The fiery death triggered by invasive infection, Adv. Immunol. 135 (2017) 81−117.

[46] L. Liu, Y. Wang, X. Guo, et al., A biomimetic polymer magnetic nanocarrier polarizing tumor-associated macrophages for potentiating immunotherapy, Small 16 (2020), e2003543.